Ultrasonics Sonochemistry 86 (2022) 106042

Contents lists available at ScienceDirect

Ultrasonics Sonochemistry

journal homepage: www.elsevier.com/locate/ultson

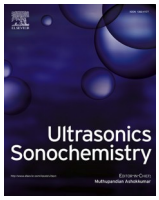

# Impulsive forces of two spark-generated cavity bubbles with phase differences

Rho-Taek Jung [a], Nyo Me Thet Naing [b,*]

[a] Foundation for Industry Cooperation, Univ. of Ulsan, 93 Daehakro, Nam-gu, Ulsan 44610, Republic of Korea
[b] School of Naval Architecture and Ocean Engineering, Univ. of Ulsan, 93 Daehakro, Nam-gu, Ulsan 44610, Republic of Korea

ARTICLE INFO

*Keywords:*
Two-bubble interactions
Phase differences
Spark generation
PVDF
Impulsive forces

ABSTRACT

The characteristics of synchronous and phase difference bubble pairs in axisymmetric configuration near a boundary are investigated experimentally by the spark discharge method. Their destructive forces on nearby boundaries are measured using a polyvinylidene fluoride sensor. The bubble pair interactions and deformed features in the boundary vicinity are dissimilar to those in bulk water. Moreover, significant discrepancies between in-phase and out-of-phase pair interactions and their intensities of impulses are also witnessed. The interbubble distance ($\eta$), stand-off distance from the boundary ($\gamma$), and phase offset ($\tau$) are crucial parameters affecting the shape evolutions and impulsive forces. From the qualitative analysis of sensor acquisition and high-speed imaging, it is observed that bubble periods are either prolonged or shorter than their corresponding isolated single cavity according to different parameters and arrangements. Additionally, the strongest impingements are produced by in-phase pairs. The impulses of phase difference bubble pairs are remarkably lower than in-phase pairs and even lower than a single bubble in some arrangements.

## 1. Introduction

Cavitation voids are generally formed when the liquid static pressure decreases below the vapor pressure in certain sites. In any real-world application, these voids or bubbles are created in large quantities, and their maximum sizes may vary; hence, different bubble periods. Upon implosion, repetitive shock waves or stresses may impose noise emission, material damage, or erosion, which reduces the efficiency of hydraulic machinery [1–6]. Although cavitation can provoke negative consequences, if one can control it effectively, the power can be harnessed and nondestructive to the system. Cavitation bubbles can be applied in various fields, such as surgical and medical procedures, cell sorting, bacterial sterilization, ultrasonic cleaning, laser cavitation peening, and ice breaking [7–13]. Laboratory-scale bubbles are often created using various methods, such as charge explosion, laser focusing, and spark discharge [14–17]. Explosion bubbles are larger, and their lifetime is longer. However, controlling the ignition time of two bubbles is challenging, and safety issues must be considered. The laser-induced bubble is highly symmetric; however, its size is relatively small, and a sophisticated, costly apparatus is essential. Since its lifetime is extremely short, an ultrafast high-speed camera is necessary. The low-voltage spark discharge method is simpler, cheaper, and reliably safe. The desired bubble size can be easily induced by controlling the electrodes' size, length, and discharge voltage. The current discharge from charged capacitors generates plasma, vaporizes the water, and creates a pulsating bubble.

Many researchers have experimentally and numerically investigated the dynamics of single bubble collapse in boundary vicinities [18–25]. Experimentally, researchers have used a schlieren system to observe the shock wave propagation, time-resolved particle image velocimetry to visualize the flow field around a cavitation bubble, hydrophone to determine acoustics transients, and extremely high-speed camera (up to 100 million frames/s) to observe the shock wave emission at very high temporal resolutions. Previous studies have shown that the impulsive pressure of the second collapse is as important as the first collapse when the bubble is near the boundary [1], the formation of a ring vortex is accompanied by a high-speed liquid jet [18], and the role of a splash in reducing first collapse impact [19]. Moreover, studies have been conducted to investigate the bubble dynamics near curved boundaries, under free surfaces, in confined channels, inside corners, and on elastic boundaries [26–29]. The evolution of bubble shapes can differ depending on the interaction with physical fields. If it is near a rigid boundary, it shows a mushroom, oval shape according to its proximity to the surface. Water domes, spikes, skirts, and spraying water films can be

* Corresponding author.

https://doi.org/10.1016/j.ultsonch.2022.106042
Received 11 October 2021; Received in revised form 3 May 2022; Accepted 15 May 2022
Available online 18 May 2022

observed if it is near the free surface.

Several studies have been conducted on two-cavitation bubbles. Two-bubble interactions in a free field have been conducted experimentally and numerically for spark-generated and laser-induced type bubbles. Blake *et al.* [30] compared numerical solutions with experimental findings of two in-phase laser-induced bubbles near a boundary for the bubble shape history (elongated bubbles, jets directed toward or away from the boundary, and bubble splitting phenomena) and the centroid motion. They found that mutual bubble interactions are as important as the nearby boundary. In the free field, Fong *et al.* [28] classified the spark-created bubble interactions according to the inter-bubble distance and phase difference. The similar-sized bubbles exhibited behavioral characteristics, such as catapult, coalescence, and jets toward and away from each other based on dimensionless parameters. Lautz *et al.* [8] reported antiphase laser-generated tandem bubble jetting experiments on microparticles for high-throughput cell sorting in microfluidic devices. They found that the directional microjet and the resultant long-lasting vortex flow can propel the particles up to 60 μm in ~ 150 μs. Han *et al.* [31] reported the experimental and numerical findings of laser-induced bubbles in bulk water. They found the maximum jet velocity of 150 m/s (of the second bubble) with a length of thrice the maximum bubble radius when out-of-phase equal-sized bubbles are generated. The first created bubble results in a slow jet of large mass that rapidly evolves into a ring vortex. Tomita and Sato [32] categorized the two-bubble interaction in reference to the bubble size ratio, interbubble distance ($\eta$), and birth time difference. They stated that the strong interaction occurs for $\eta < 1$, followed by several phenomena, including bubble penetration, jet formation, toroidal bubble collapse, and high-speed fine jet formation. They also indicated that conical-pulsed jet formation is similar to a water spike when a single bubble expands under a free surface. Robles *et al.* [33] conducted investigations of double bubble jetting on soft materials (agar gel-based skin phantom and soft paraffin). They selected an antiphase difference pair with $\eta = 0.74$, since this configuration produces the longest penetration length on the target material. They stated that the surface damage could be reduced to 45%, compared with single bubble impingement, and is appropriate for needle-free applications.

Previous studies have conducted pressure measurements for single bubble dynamics. In the studies by Wang and Chen [23] and Tomita and Shima [1], the small valley in the pressure output profile of the first collapse was evident for $0.6 <$ stand-off distance from the boundary ($\gamma$) $< 1.1$. Tong *et al.* [19] conducted laser-induced experiments and numerical simulations for $0.8 \leq \gamma \leq 1.2$ to explain this phenomenon. According to them, the jet impact on the thin liquid layer between the bubble and the boundary causes radial flow outward from the jet axis, which collides with the inward liquid motion induced by the collapsing bubble, resulting in an opposite-directed splash of the jet. Their computations showed that the jet impact pressure is ten times less than that of a splash. This argument was further endorsed by Shaw *et al.* [20]; experiments on laser-created bubbles for $0.56 \leq \gamma \leq 1.5$ were performed with a variable maximum radius and a fixed distance from the boundary. The upper and lower limits were 1.04 and 0.58 for the two main peaks associated with the splash effect, respectively. Brujan *et al.* [21] also reported the final stage of bubble collapse for $\gamma = 0.9$ and 1.1 recorded at 5 million frames/s. They concluded that a large part of the kinetic energy of the radial flow into the main bubble is transformed into the kinetic energy of a rotational flow around the cavity next to the wall. Their experimental and numerical investigations reveal that their assertion accompanying the splash may explain the low damage potential caused by the first bubble collapse near the boundary when $\gamma \approx 1$. Yao *et al.* [24] utilized the Hopkinson pressure bar as the sensing element to acquire the pressure waveform induced by spark-generated bubble collapse loading. The peak pressure loading against the stand-off distance decreased monotonically with the increasing distance.

The interactions of two bubbles, both in- and out-of-phase, in the context of migratory behaviors, bubble shape history, and jet formations have been elucidated to some extent by previous studies. Nonetheless, the impingement characteristics of these bubble pairs on the boundary still need to be unraveled. This study contributes to the qualitative analysis of similar-sized tandem bubbles produced simultaneously or with phase difference by the spark method. The experimental setup and the polyvinylidene fluoride (PVDF) sensor calibration are provided in Section 2. Sections 3 and 4 investigate a single- and two-bubble collapse near boundaries, respectively. Next, in Section 5, the non-dimensionalized bubble period is presented. Furthermore, Section 6 investigates the impulsive force on boundaries, and Section 7 concludes the study.

## 2. Experimental setup

Fig. 1 depicts the experimental setup schematic. Experiments were conducted in a water tank of dimensions (400 mm × 400 mm × 450 mm) filled with tap water up to 400 mm at room temperature. Two spark discharge circuits are inspired by Goh *et al.* [17]. An N-channel metal–oxide–semiconductor field effect transistor (MOSFET) (IXYS IXFH75N10) was used to discharge the energy stored in the capacitors (6900 μF). The tinned copper wire electrodes of 0.1 mm, which are in contact initially, are connected to low-voltage discharge circuits. As described in the figure, two pairs of cross electrodes are positioned horizontally adjacent to the vertical wall. The maximum bubble radii induced by this configuration are between 2.37 and 6 mm. Hence, the interference from thin electrodes, which are>20 times smaller than the bubble, is neglected. Two separate circuits were employed to induce bubble pairs independently. The backlight source (200 W) is used for illuminating the high-speed camera through a translucent acrylic sheet. Images are recorded with a Chronos 1.4 high-speed camera at 32,667 frames/s. To quantify the impulse signals produced by the cavitation bubble collapse, a thin film (28 μm) of PVDF piezoelectric transducer (FDT1-028 K) is attached to a marble block next to the spark. The sensor is connected directly to an oscilloscope (PICOSCOPE 5443D, 100 MHz, maximum sampling rate 1GS/s). NI LabView Graphical User Interface is applied to interact with NI cRIO-9047. The cRIO sends out synchronous trigger signals to two spark circuits, a high-speed camera, and an oscilloscope. A large current flows between the positive and ground terminals within a short MOSFET switch time (which is set as 400 μs herein). Then, plasma is created, accompanying the release of intensive white light. The nonequilibrium bubble comprising gaseous products and liquid vapor is generated. Electrodes from both terminals are cut (evaporated at the crossing point) after short circuiting so that new electrode pairs are needed for every new experiment. Moreover, the contact area of the two electrodes, the electrodes' connection to the main wires of the circuit, and the slight voltage inconsistency during the instant discharge contribute to the precision of the bubble size.

The PVDF film has a sensing area of 12 mm × 30 mm printed with

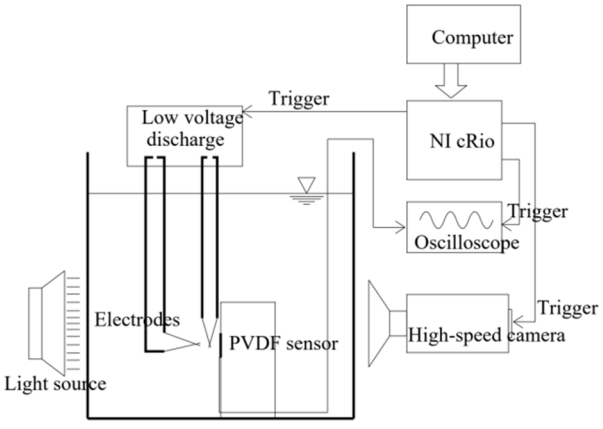


**Fig. 1.** Schematic of the experimental setup.

long silver ink electrodes on both surfaces of the die-cut polymer substrate (28 μm thick). Connector pins are at the end of the 100-mm-long silver electrodes for the signal output. The sensitivity is estimated as 0.013 V/N by the manufacturer. Herein, the sensor is laminated with a 50-μm-thick film for protection and waterproof purposes so that the sensitivity may be changed according to the protection layer thickness and the material to which the sensor is attached. The ball drop method uses stainless steel balls (0.52, 0.892, 1.416, 2.126, and 3.023 g) released from a 500 mm height from the top of an acrylic-guiding tube (Fig. 2(a)). The impulse–momentum theorem equation proposed by Hujer and Müller [34] is used to calculate the mean impact force:

$$F_{mean} = \frac{1}{t}\int_{t_1}^{t_2} F(t)dt = \frac{m}{t}(v_1 + v_2) \quad (1)$$

where $v_{1,2} = (2gh_{1,2})^{1/2}$, $h_{1,2}$ are the heights, and $g$ is the gravitational acceleration. The $m$ and $t$ are the mass of steel balls and the impact duration of the sensor signal. The maximum force is twice the mean force ($F_{max} = 2F_{mean}$). Fig. 2(b) presents the calibration results. The sensitivity value is 0.0183 V/N, which exceeds the factory estimated value due to the additional layer for damage protection and waterproofing. Fig. 2(c) plots present an example of the signal output of a 1.416 g ball drop test. After three experiments, the average maximum voltage and pulse duration are 3.33 V and 75 μs. Evidently, the measured voltage has a strong linear correlation with the impact force on the sensor. The PVDF film exhibits a rise time as fast as 56 ns and a flat frequency response ranging from 0 to 1 MHz when testing in a gas dynamic shock tube Wang and Chen [23].

## 3. Single bubble dynamics with an impulsive force

The single bubble is placed near the rigid vertical boundary at a distance of $d$ between the wall and the bubble inception point. The proximity parameter, $\gamma = d/R_{max}$ (where $R_{max}$ is the Rayleigh collapse time), plays an essential part in the magnitude of the impact force on a solid boundary. The same bubble radius or $d$ can be maintained to achieve variable $\gamma$. For a single bubble collapse, the approaches with a 4.55 mm fixed radius ($R_{max}$) and a 5 mm fixed distance (d) from the wall were applied. Fig. 3(a) plots the maximum bubble sizes created from 40 to 70 V in the free field; each point represents three repetitions. The bubble shape evolutions are depicted in Fig. 3(b) and (c) for $\gamma$ with a fixed radius and fixed $d$, respectively. The first frames of each $\gamma$ are the instants when bubbles reach maximum volume. The first implosion moments are in the second frames, followed by maximum rebounded cavities. An aspherical collapse accompanied by the jet penetration at the top section of the bubble can be clearly observed when $\gamma < 1.1$. These features indicate that the boundary disturbs the fluid flow and strongly influences the growth and collapse phases of the bubble dynamics.

Fig. 3(d) shows the maximum impulsive forces generated from the first and second collapses and the impulses according to their corresponding proximity parameter with the same radius. Evidently, the smallest $\gamma$ gives the largest force reading for the first collapse, $\gamma = 0.44$. The second collapse forces when $\gamma \approx 1.0$ are marginally higher than the first collapse outputs, which agrees with the experimental findings of Wang *et al.* [22] and Tomita and Shima [1]. In their studies, the small valley in the pressure output of the first collapse is evident when $0.6 < \gamma < 1.1$. Afterward, the first collapse impacts exceed those of the second collapse. The rises in force trends are noticeable when $3 < \gamma < 3.5$, which eventually decreases as $\gamma$ increases. The impulses are determined using Equation (2):

$$I = \int_{t_1}^{t_2} F(t)dt \quad (2)$$

The impulses from the bubble collapse (first, second, third, and fourth, if significant) are added together, 0.5–3.5 ms, from the sensor outputs. The typical impulse lasts for 0.1–0.2 ms and can be shorter or longer in some cases. The maximum impulse reaches approximately 47 Nms (newton milliseconds) when $\gamma = 0.88$. When the slope of the downward graph trend is steep when $\gamma < 3.5$, a more stable trend is witnessed. Fig. 3(e) depicts the maximum impact forces and impulses for varying bubble radii. The second collapse impacts are more pronounced when $0.8 < \gamma < 1.1$, which is similar to the first method. By contrast, the impulses drastically reduce as $\gamma$ increases. The maximum impulse is recorded as 83 Nms at $\gamma = 0.83$. It is indeed obvious that bigger bubbles collapse more destructively near the boundary than smaller ones.

To analyze the characteristics of the collapse time, Fig. 3(f) plots the time series of each $\gamma$. Evidently, the collapse times increase as $\gamma$ decreases, and the second peaks become more observable. The time intervals between the birth instant and the first collapse and between the first and second collapses are denoted as $T1$ and $T2$, respectively. These periods are normalized by the $R_{max}$,

$$T_{coll} = R_{max}[\rho/(p_\infty - p_v)]^{1/2} \quad (3)$$

where $p_\infty$, $p_v$, and $\rho$ are the static pressure, vapor pressure, and density. In an infinite incompressible fluid, neglecting surface tension and gas content, the Rayleigh bubble is 1.83. However, this statement is violated in the boundary proximity (Fig. 3(g)). Closer to the boundary, $T1$ escalates, although the last point decreases, with a value closer to the free field. The maximum and minimum periods are ~ 2.05 and 1.93, respectively; it is expected to converge to the free field bubble as $\gamma$ increases. A comparable manner of the declining curve is also witnessed for $T2$, with 0.47 and 0.17 as the highest and lowest periods. Many researchers have studied the dynamics of single bubble collapse experimentally and numerically, so a detailed presentation will be excluded herein [1,19,21,23].

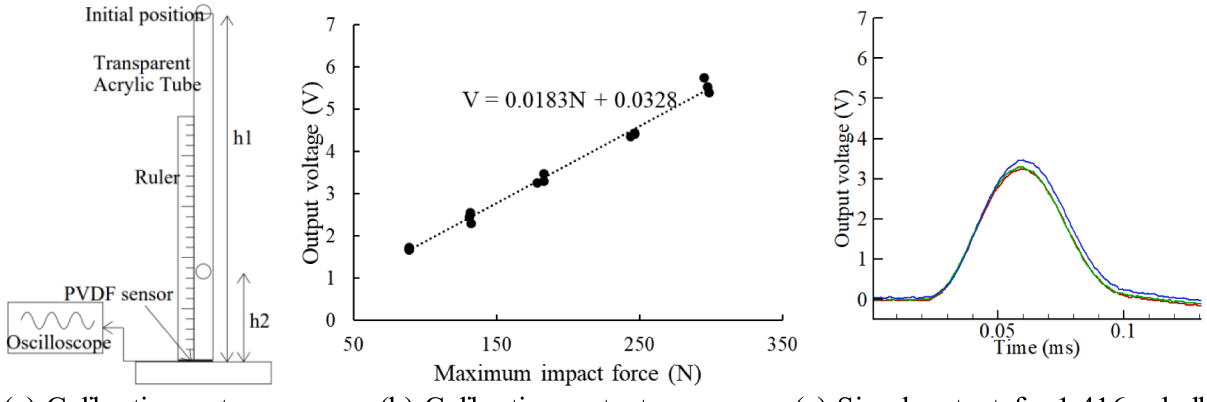


**Fig. 2.** PVDF sensor calibration.

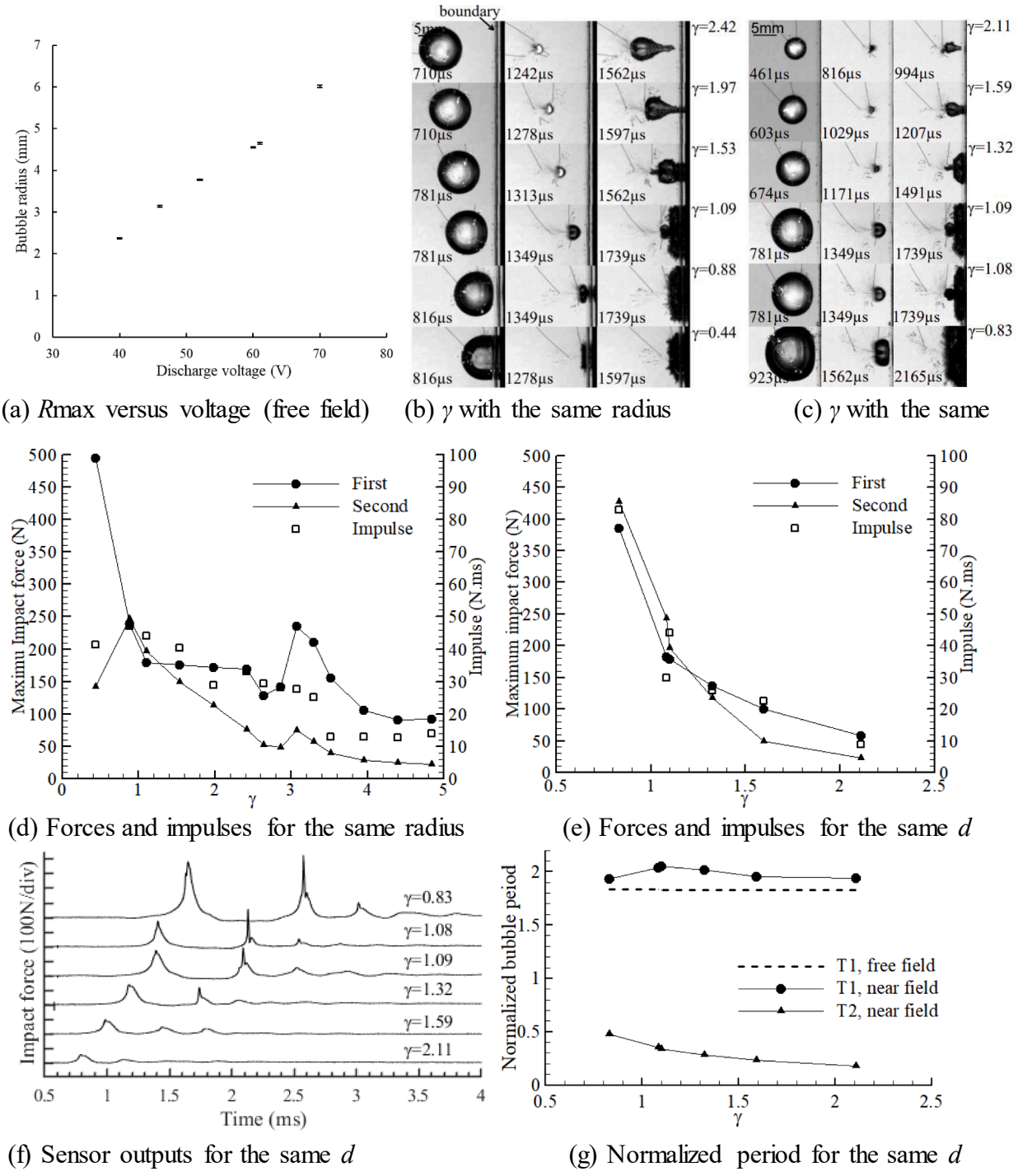


(a) *R*max versus voltage (free field) (b) $\gamma$ with the same radius (c) $\gamma$ with the same

(d) Forces and impulses for the same radius (e) Forces and impulses for the same *d*

(f) Sensor outputs for the same *d* (g) Normalized period for the same *d*

**Fig. 3.** Single bubble collapse as a function of $\gamma$.

## 4. Two-bubble dynamics with an impulsive force

Fig. 4 illustrates the schematic arrangement of two bubbles in the vicinity of the rigid vertical boundary. The distance between the boundary and the birth point of bubble 1 (B1) is $d1$. Next, the distance between B1 and the birth point of bubble 2 (B2) is $d$. Furthermore, the distance between the wall and B2 is $d2$. The dimensionless parameters are as follows: $\gamma_1 = d1/R_{max,1}$, $\gamma_2 = d2/R_{max,2}$, $\eta = d/(R_{max,1} + R_{max,2})$, and phase offset $(\tau) = \Delta t/T_{osc}$, where $\Delta t$ is the time gap between the first and second generated bubbles, and $T_{osc}$ is the length of time from the inception of bubble 1 to its first collapse. The radii of similar-sized bubbles, B1 and B2, are 4.62 and 4.55 mm, respectively. Experiments were conducted with two main cases, cases A and B. For case A, the fixed B1 is created at 5 mm ($\gamma_1 = 1.08$) away from the wall when B2 varies with $d$, and it is either synchronized with B1 or is induced with a time lag (Fig. 4(a) and (b)). For case B, B1 is placed at 22 mm ($\gamma_1 = 4.76$) away from the wall when B2 varies with $d$ and is either synchronized with B1 or is induced with a time delay (Fig. 4(c) and (d)). In Fig. 4(e) and (f), the sensor signals for five consecutive discharges of the single B1 of cases A and B are displayed, respectively. The inserts show the first impact deviation from the raw sensor signals at a higher temporal resolution. From averaging five repetitive experimental data, the $T_{osc}$ values for cases A and B are 1.40 and 1.27 ms, respectively. Once the periods for both cases are determined, the phase differences between the bubbles

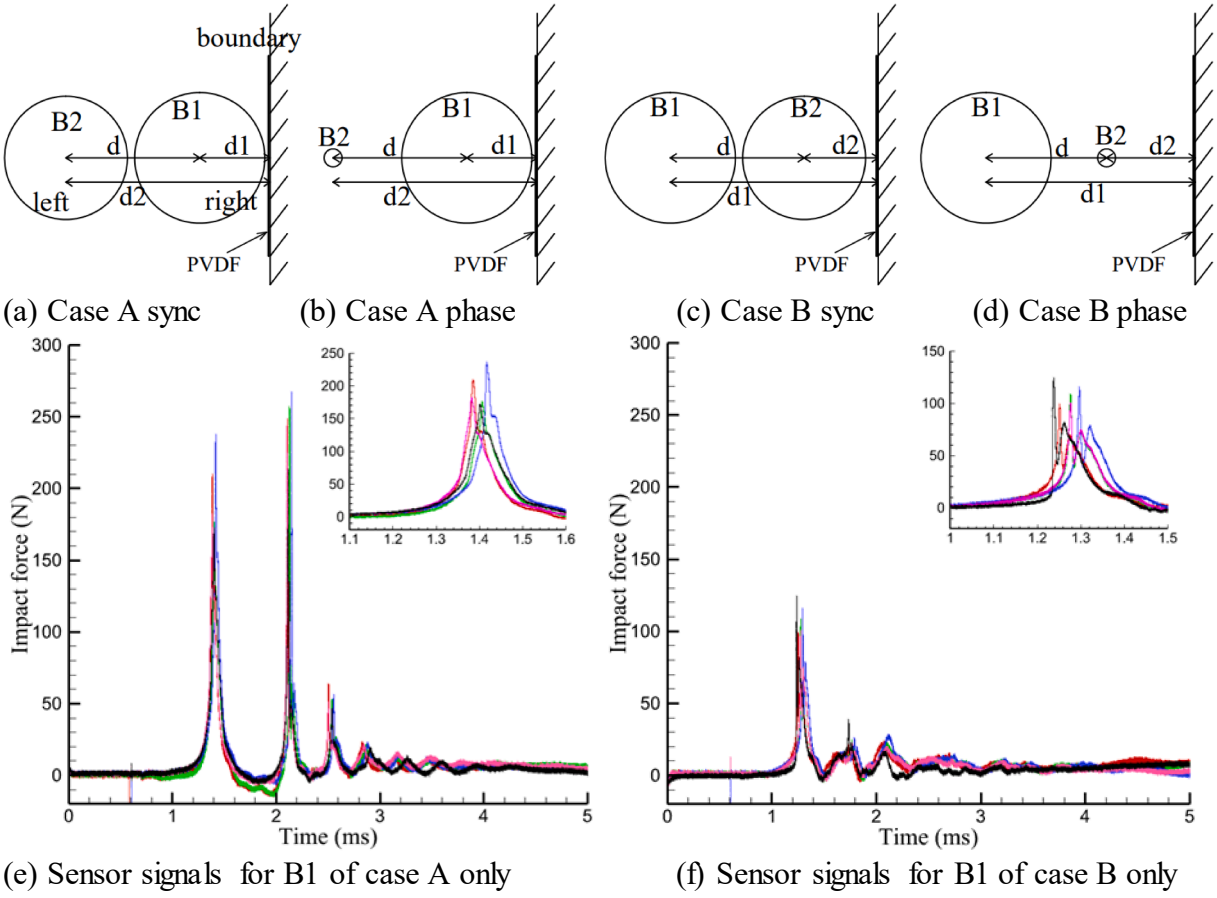


**Fig. 4.** Arrangements of reference bubble 1 (B1) and adjustable bubble 2 (B2) near the boundary.

are set based on B1. The value of $\eta$ varies from 0.7 to 1.9 for all cases. It is apparent that with a large gap between the bubbles, a weak interaction occurs between them although the adjacent bubble is strongly influenced by the nearby boundary. Therefore, the distant bubble collapses spherically in the free field, whereas the adjacent bubbles exhibit the characteristics of a single bubble collapse near the boundary. When two bubbles are brought closer, implying smaller $\eta$, different bubble-deformed shapes are observed, resulting from the boundary influence and mutual bubble interaction. The evolution of the shapes and plausible causes are discussed as follows:

### 4.1. Case A with $\eta = 1.63$

Fig. 5 presents the bubble shape evolutions and comparison of sensor outputs of case A according to their temporal separation for $\eta = 1.63$. When the in-phase ($\tau = 0$) bubbles are placed relatively apart from each other, B2 behaves in the manner of a single bubble collapse, whereas B1 is affected by both the boundary and B2 in such a way that it is stretched to form a high curvature surface (1.38 ms of Fig. 5(a)). Since they are similar in size, both bubbles enter the collapse phase almost concurrently. However, unrestricted inward flow to B2 facilitates its swifter shrinkage than B1. From the B1 perspective, the inward flow is only available from the sides as the fluid from the left part is pulled by B2, whereas the right boundary hinders any motion. This phenomenon elucidates the deformation of elongated B1. Afterward, rebounds of B2 migrate toward the boundary. When B2 is generated with $\tau = 0.285$, the first created bubble (B1) could not reach its maximum volume, as shown in the 0.64 ms of Fig. 5(b). It can be postulated that the shock wave from delayed the bubble generation and its outward flow during expansion interferes with the growth stage of B1 and coerce it to shrink earlier than the isolated B1. B2 contracts when the first bubble is on the verge of implosion. The outward flow from the rebound of B1 promotes delayed bubble contraction speed and collapse opposite the boundary. The superposition of its collapse and shrinkage of the remnants of B1 (tiny, disintegrated bubbles) produce noticeable small bubbles on the flat surface of B2 rebound (1.74 ms of Fig. 5(b)). This feature is seen for $1.42 < \eta < 1.85$. The second collapse of the delayed bubble merges with a small bubble and ultimately travels away from the boundary. A similar procedure is observed for the antiphase pair, $\tau = 0.5$, except that the first bubble now achieves a bigger volume than the smaller $\tau$ (Fig. 5(c)). The impacts of single bubbles on the boundary are compared with the in-phase bubble pair in Fig. 5(d). It can be confirmed that the lifespan of the bubble shortens as $\gamma$ increases when the profiles of two-single bubbles are compared. Evidently, the first collapse of the bubble pair is more destructive (300 N) than the counterpart of the single B1 (182 N), whereas the second peaks are the other way around. Moreover, the mutual bubble interaction prolongs the period between the first and second peaks. The magnitudes of peaks recorded for the out-of-phase bubble pairs are relatively smaller than the synchronized pairs or single B1 (Fig. 5(e)). The first created bubble of a shorter phase difference pair collapses faster (1.22 ms) than the antiphase pair (1.39 ms), because of its smaller size. Afterward, the first collapse of B2, the second collapse of B1, and the second collapse of B2 occur sequentially. From the sensor profiles, the peaks of B1 are more striking than the delayed bubble peaks. Furthermore, the second peaks of B1 for both $\tau$ values are ~ 170 N. Compared with a single B1, B2 makes the impact time of the pair retarded, advanced, and resembled when $\tau$ = 0, 0.285, and 0.5, respectively.

### 4.2. Case A with $\eta = 0.76$

Bubble deformations and comparison of sensor outputs of case A for

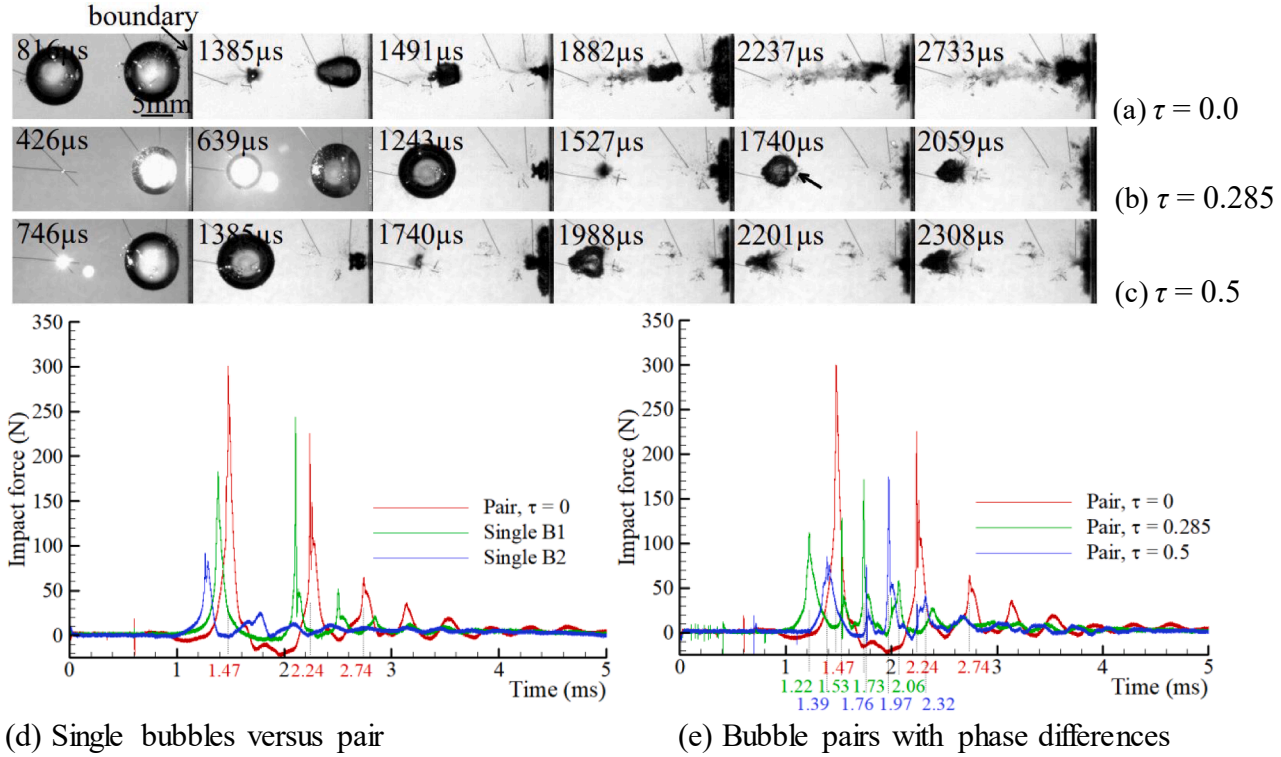


**Fig. 5.** Bubble interactions of case A for parameters: $\gamma_1 = 1.08$, $\gamma_2 = 4.4$, and $\eta = 1.63$. Evolution of bubble morphology for $\tau$ = (a) 0, (b) 0.285, and (c) 0.5. (d) Comparison of sensor outputs for bubble pair with $\tau = 0$ (red), single bubble 1 (green), and single bubble 2 (blue). (e) Comparison of sensor outputs for bubble pair with $\tau = 0$ (red), 0.285 (green), and 0.5 (blue). Boundary is placed on the right side of each picture here and subsequently.

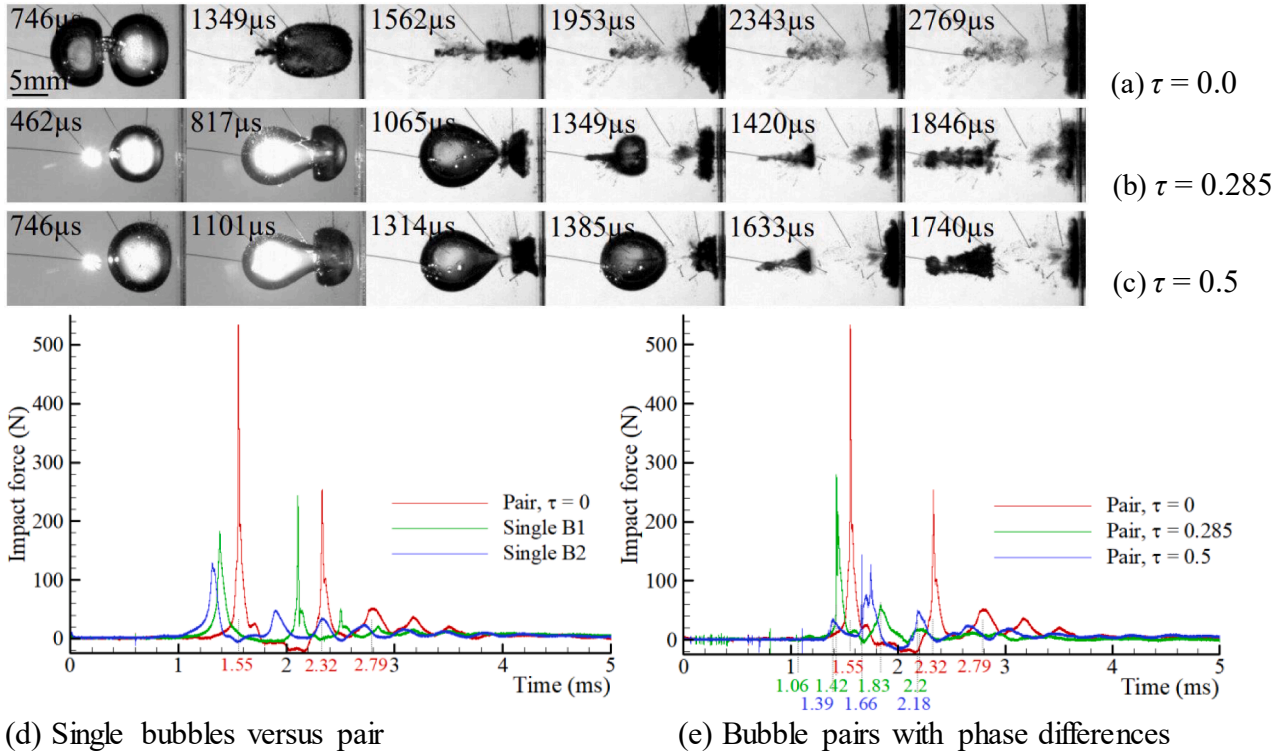


**Fig. 6.** Bubble interactions of case A for parameters: $\gamma_1 = 1.08$, $\gamma_2 = 2.63$, and $\eta = 0.76$. Evolution of bubble morphology for $\tau$ = (a) 0, (b) 0.285, and (c) 0.5. (d) Comparison of sensor outputs for bubble pair with $\tau = 0$ (red), single bubble 1 (green), and single bubble 2 (blue). (e) Comparison of sensor outputs for bubble pair with $\tau = 0$ (red), $\tau = 0.285$ (green), and $\tau = 0.5$ (blue).

$\eta = 0.76$ are illustrated in Fig. 6. For the synchronized pair (Fig. 6(a)), B1 expends with the left and right flattened profiles since it is sandwiched between the growing B2 and rigid boundary. After B2 attains its maximum volume at 0.75 ms, the growing B1 is further lengthened by the contracting flow of B2. Despite the rapid shrinkage of B2, the contraction of B1 is comparatively slow, and the thin water film between the bubbles rupture. When B2 collapses, spray formation and jet penetration through B1 cause its surface to burst and expedite implosion. However, the bubble pairs with a time lag exhibit different deformation characteristics (Fig. 6(b) and (c)). Upon creating a delayed bubble, the first generated bubble can no longer expand although it has not reached its maximum volume. Hence, a shorter time gap delivers a smaller B1 than a larger time gap. First, the growing B2 forces the first bubble to shrink, forming a dent on the first bubble surface at the early stage. This dent, conical water mass, is later filled by the tip of the elongated delayed bubble until it collides with the opposite wall of the first bubble. The toroidal collapse of B1, which produces a high-pressure compressive wave, inverts the sharp conical wall of B2, creating a water jet inside and escalating its collapse. Afterward, B2 rebounds and collapses severally, and travels away from the boundary. Acquired sensor waveforms are compared in Fig. 6(d) and (e). Apparently, the concurrent bubble pair is much more detrimental than single bubbles; their first peaks are 530 N for the pair, approximately 182 N for the near bubble, and 128 N for that which is distant. The second peak of B2 is significantly low, whereas B1 and the pair show similar readings over 240 N. For the out-of-phase bubble pairs, the first collapse of B1 is hardly felt by the sensor, 1.06 and 1.39 ms for $\tau = 0.285$ and 0.5, respectively. The first collapse of the delayed bubble was measured as 280 N for the smaller $\tau$ and 145 N for the antiphase pair. Overall, imposing phase differences on this bubble pair configuration markedly diminished the impact on the boundary.

### 4.3. Case B with $\eta = 1.42$

Fig. 7 presents the bubble pair interactions and force profile comparisons for case B with $\eta = 1.42$. In this bubble pair arrangement, B2 is sited closer to the boundary than to B1. Nevertheless, B2–B1 reveals stronger interaction than B2–boundary in Fig. 7(a) for the contemporary pair. The inward flow to the shrinking of B1 and the boundary yields an elongated contraction of B2. Following the collapse of B1, the right part of B2 collapses first since more flow is accessible from that direction. Thus, the occurrence of jets toward each other is observed. The event of jetting to the boundary of both bubbles is also observed when $\eta > 1.42$ for this configuration. The rebound bubbles coalesce into one and migrate to the boundary. The bubble–bubble mutual interaction is weaker in-phase difference bubble pairs. The delayed bubble is not stretched discernibly by the shrinking of B1 (Fig. 7(b) and (c)), although its (contracting B2) left wall is flattened by the rebound of B1. Eventually, pulsating cavities repel one another and travel in opposite directions. The single bubble impingements are much weaker than the pair impact on the boundary, as evident in Fig. 7(d), 366 N (pair), 170 N (B2), and 110 N (B1). B1 is located far from the boundary, and B2 debilitates its impact on the boundary (sensor). The sensor recordings show that at 1.06 and 1.19 ms, $\tau = 0.315$ and 0.5, respectively (Fig. 7 (e)). The maximum peaks of the phase difference pairs are 340 and 250 N, respectively. The significant peak impact time of the pairs (for all $\tau$) exceeds the period of the single B1 because of elongated B2 ($\tau = 0$), cushioning the collapse of B1 by B2 ($\tau = 0.315$ and 0.5).

### 4.4. Case B with $\eta = 0.76$

Fig. 8 depicts the bubble shape evolutions and comparison of sensor outputs of case B according to their temporal separation for $\eta = 0.76$. Synchronous bubble pair deformation is analogous to single bubble dynamics near the boundary, manifesting flattened proximal walls along the midplane and hemispherical distal walls as they reach maximum volumes. The thin liquid film persists until two cavities collapse independently along with liquid jets toward each other (1.45 ms of Fig. 8(a)). Rebound bubbles merge into a coalesced bubble and pulsate at the same position severally. By contrast, out-of-phase bubble pairs evolve comparably with case A of the same $\eta$ parameter (Fig. 6(b) and (c)). The wide conical tip of the delayed bubble protrusion to the first bubble, the toroidal collapse of the first bubble, the inverted sharp tip of B2 coupled with spray formation and water jet inside, and the B2 implosion appear in an orderly manner. Both bubbles rebound and collapse for several circles and migrate away from each other. Robles *et al.* [33] conducted double bubble jetting experiments directed toward soft paraffin and an agar gel phantom and reported the parameters as $\gamma_2 = 3.5$, $\eta = 0.75$, and $\tau = 0.5$. They concluded that a longer penetration length and a smaller

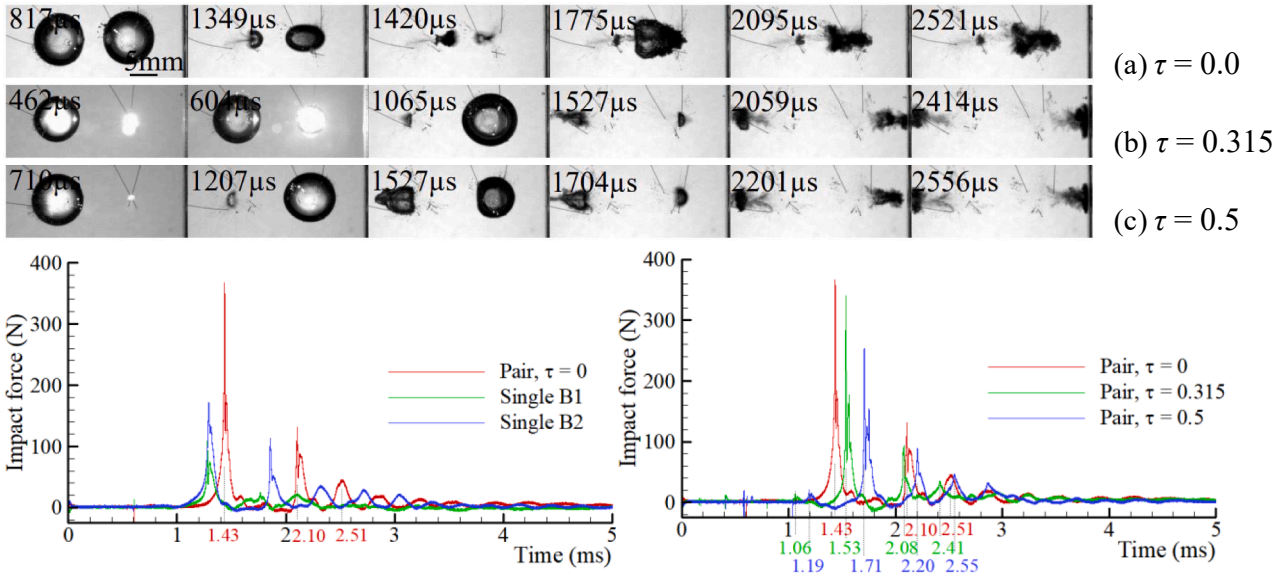


**Fig. 7.** Bubble interactions of case B for parameters: $\gamma_1 = 4.76$, $\gamma_2 = 1.98$, and $\eta = 1.42$. Evolution of bubble morphology for (a) $\tau = 0$, (b) $\tau = 0.315$, and (c) $\tau = 0.5$. (d) Comparison of sensor outputs for bubble pair with $\tau = 0$ (red), single bubble 1 (green), and single bubble 2 (blue). (e) Comparison of sensor outputs for bubble pair with $\tau = 0$ (red), $\tau = 0.315$ (green), and $\tau = 0.5$ (blue).

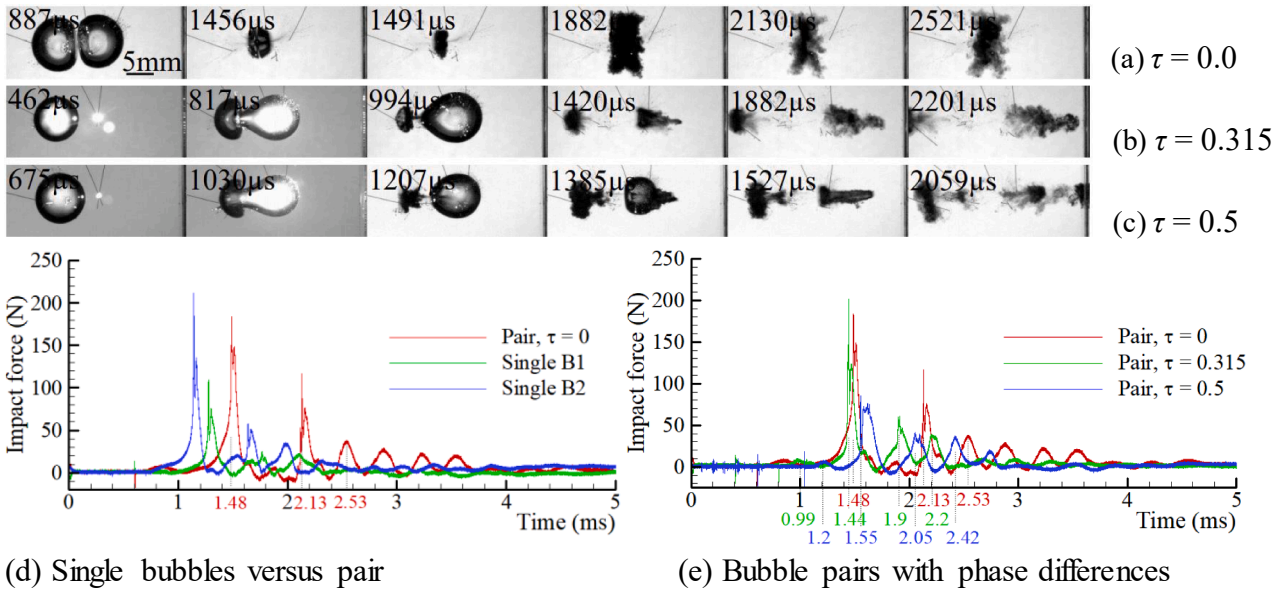


**Fig. 8.** Bubble interactions of case B for parameters: $\gamma_1 = 4.76$, $\gamma_2 = 3.29$, and $\eta = 0.76$. Evolution of bubble morphology for $\tau =$ (a) 0, (b) 0.315, and (c) 0.5. (d) Comparison of sensor outputs for bubble pair with $\tau = 0$ (red), single bubble 1 (green), and single bubble 2 (blue). (e) Comparison of sensor outputs for bubble pair with $\tau = 0$ (red), $\tau = 0.315$ (green), and $\tau = 0.5$ (blue).

damage area on the target material could be assured by employing an antiphase bubble jet. The comparable results are also observed in this study with similar parameters. The microjet penetration length is the longest among all the test conducted, and its impact loading is smaller than in-phase and shorter phase different pairs. As shown in Fig. 8(d), the first peak force of the in-phase pair is < single B2, 180 N, and 210 N, respectively. The sensor output of the coalesced cavity fluctuates longer, with a significant amplitude than single bubbles. The force profile of a shorter temporal gap achieves a higher first peak (201 N) than the simultaneously generated pair (180 N) and antiphase pair (85 N), Fig. 8 (e). Note that these first peaks are the first collapse impacts of delayed bubbles rather than toroidal collapses of B1, which marks at 0.99 and 1.2 ms for $\tau = 0.315$ and 0.5, respectively. The sensor barely detects the existence of B1.

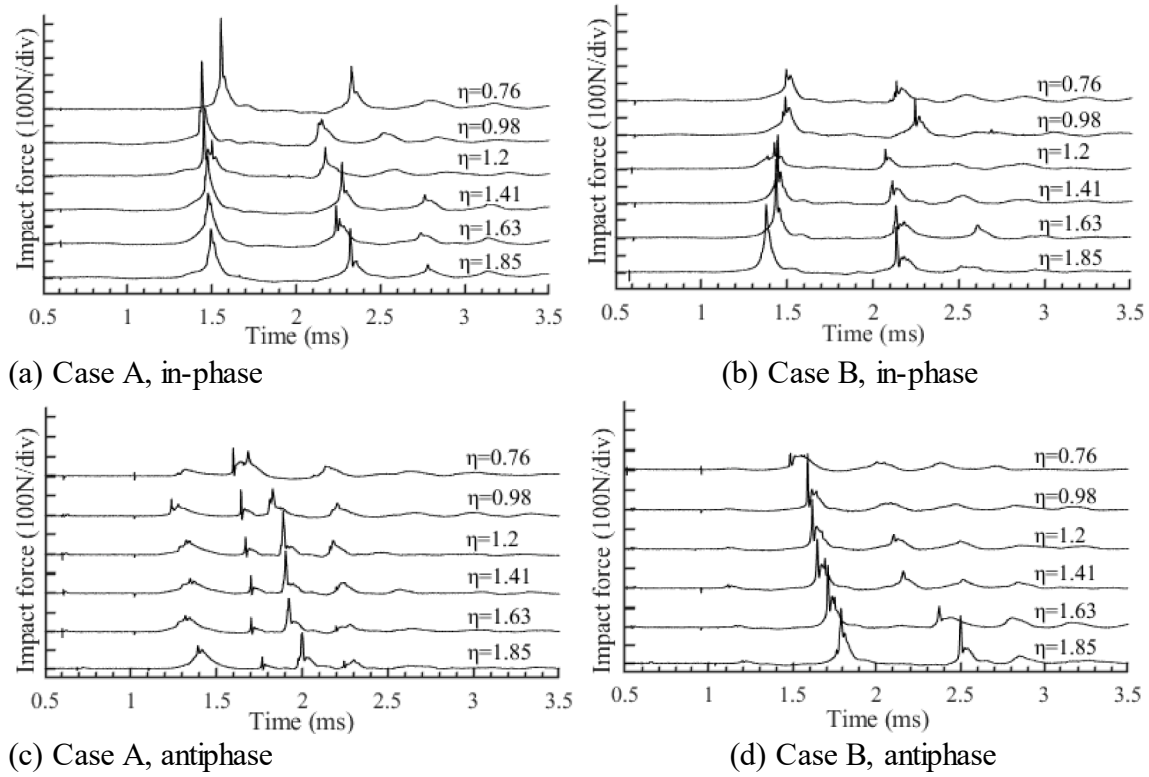


**Fig. 9.** Sensor signals of in-phase bubble pairs for cases (a) A and (b) B. Antiphase pairs for cases (c) A and (d) B.

## 5. Nondimensionalized bubble collapse period

### 5.1. Time series of two-bubble interactions

To further analyze the bubble interaction as a function of $\eta$, the output sensor profiles of cases A and B when $0.76 < \eta < 1.85$ are compared in Fig. 9. First, the most indisputable fact is the strongest impacts are delivered by concurrent case A, which is followed by the concurrent case B, antiphase case B, and antiphase case A. Evidently, in case A, fixed B1 is created near the boundary, whereas B2 becomes closer to B1 with $\eta$; hence, the maximum impact forces become prominent as $\eta$ decreases (Fig. 9(a)). Inversely, in case B, fixed B1 is incepted at the farthest from the boundary, whereas B2 moves toward B1 as $\eta$ increases; therefore, the largest $\eta$ (B2 closest to the boundary) gives the largest impact than the smaller $\eta$ (Fig. 9(b)). Additionally, mirror bubbles (Fig. 8(a)) need more time to implode with smaller $\eta$. The intensities of in-phase cases are discussed thoroughly in the next section. For phase difference case A, the first collapse of B1 hits the boundary with a fairly wide pulse than the counterpart of B2; the fast-rising narrow pulse of B2 is as swift as 10 μs (Fig. 9(c)). Given that B1 is closer to the boundary and its $\gamma$ is $\sim$ 1.0, the second peaks are higher than the first, and the pulse width is slender at the tip and broad at the base. In this configuration, the impingements of B2 are properly captured by the sensor, but their pulses are very short-lived compared to their height. The remnants of B1 between B2 and the boundary can be pointed out as the possible reason. In Fig. 9(d), the first peaks of the phase difference case B are much more prominent than the second peaks. More interestingly, these peaks predominantly result from B2. The sensor barely registers the impacts of B1. Considering the period, in all cases, the first collapse times reveal either increasing or decreasing track in the function of $\eta$. By contrast, the second peaks of synchronous pairs strike the boundary chaotically, and a more orderly manner is displayed by the second peaks of the antiphase pairs.

### 5.2. Collapsing time

From sensor acquisition and high-speed photographs investigations, the tendency of bubble pair collapse periods against $\eta$ is plotted in Fig. 10. $T1$ is the duration of the birth instant and first collapse, and $T2$ is the duration between the first and second collapses. These periods are nondimensionalized by the $R_{max}$ (Section 3). Fig. 10(a) presents the comparison of the $T1$ values of case A for single bubbles and in-phase and antiphase pairs. B1 of antiphase pairs fluctuates around single B1 with little variation, but B1 of the simultaneous pairs took longer than single B1. It somehow decreases as $\eta$ decreases, except for the last point. At the shortest inter bubble separation of the in-phase pair, the sudden surge of B1 accounts for the strong mutual bubble interaction (Fig. 6(a)), which also speeds up the first collapse of B2. B2 of the in-phase pairs shows a downward trend toward the boundary, and the value is greater than single B2. Phase difference B2 also falls gradually approaching the boundary, and it is clearly the highest curve. Different aspects of B1 are detected for $T1$ of case B (Fig. 10(b)). Antiphase B1 collapses quicker (smaller radius) than single B1 showing a noticeable gap between them. Meanwhile, B1 of the in-phase pairs increases and visibly deviates from single B1 as B2 approaches it, manifesting stronger interaction. Consequently, B1 and B2 of concurrent pairs collapse almost simultaneously at a closer bubble distance, verified by the B2 in-phase line. Contrarily, antiphase B2 and single B2 decrease with steeper slopes as it is placed away from the boundary. The second collapse time ($T2$) of case A for single B1 and in-phase B1 is relatively closer than that for antiphase B1 (Fig. 10(c)). Antiphase B1 collapse is swifter with drastically reduced time for the smallest $\eta$, and it can be concluded that the phase offset in this bubble arrangement unquestionably shortens the lifetime of B1. Antiphase and single B2 hit the boundary at a similar time, but in-phase

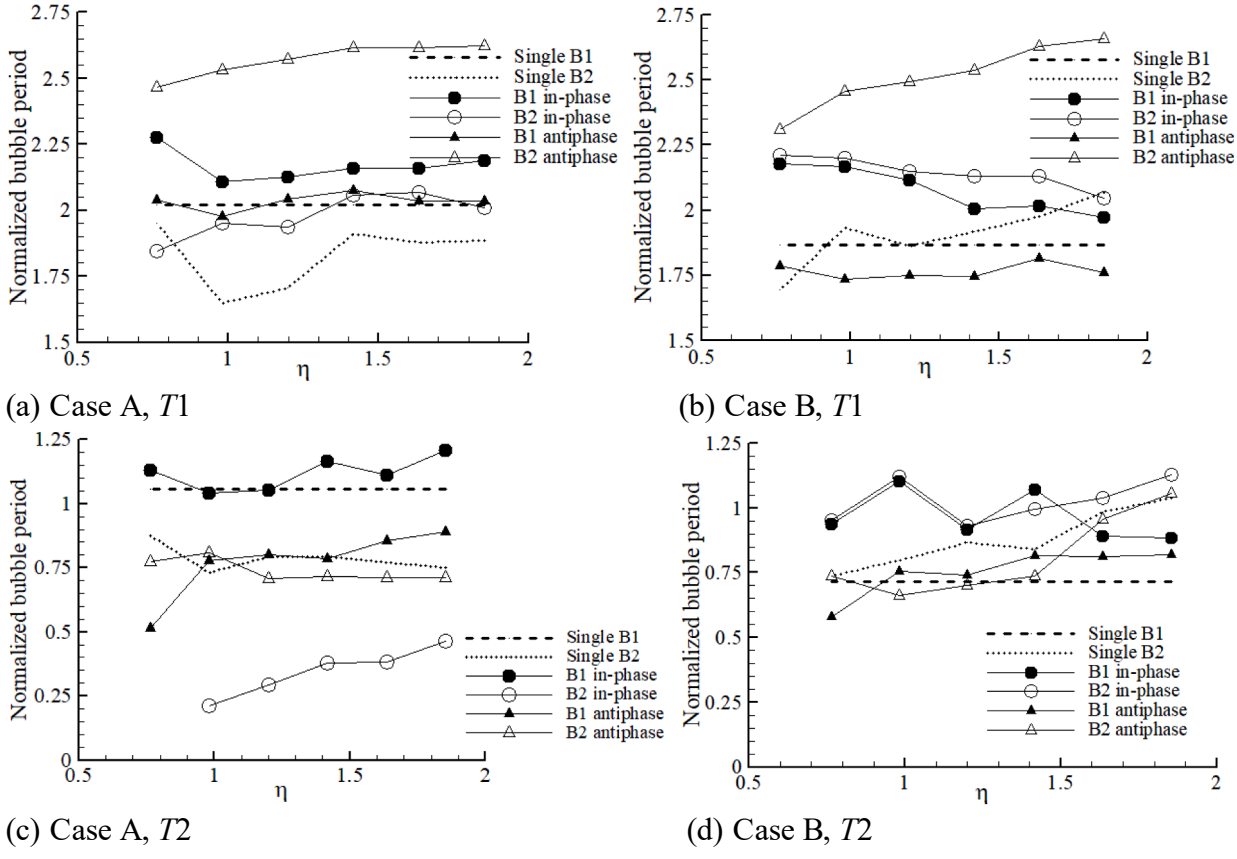


**Fig. 10.** Normalized bubble period of $T1$ for (a) case A and (b) case B and $T2$ for (c) case A and (d) case B, as a function of $\eta$.

B2 vanishes much faster, and its life span is the shortest for this arrangement among all cases. Fig. 10(d) reveals that for $\eta > 1.41$, $T2$ of case B of single, antiphase, and in-phase B1 are in ascending order with some gap between them. Beyond that $\eta$, phase offset B1 resembles single B1 and falls sharply to the last point. However, in-phase B1 is more of an up and down feature, always higher than single B1, and it merges with B2 later. Evidently, the second collapse of in-phase B2 exceeds the antiphase or single B2. When B2 is closer to the boundary, the three bubbles have not much difference in magnitude. Then, single and antiphase B2 drop significantly and become closer to the single B1 value as $\eta$ decreases. The comparison of cases A and B for both collapse periods shows that the synchronized period of B1 exceeds that of single and antiphase B1, and the synchronized period of B2 exceeds that of single B2, except for the $T2$ curve of case A. Phase difference B1 is lower than single B1 for $T1$ and $T2$ of cases A and B, respectively, but above or below the rest of the cases. Clearly, $T1$ of antiphase B2 is highest for both cases, and $T2$ is similar to that of single B2.

## 6. Impulsive forces of two-bubble interactions

Fig. 11(a) and (b) present the maximum impulse forces generated by the first and second collapses of synchronized pairs for cases A and B, accompanied by their corresponding single bubble collapse forces. In case A, the most distinguishing trend line is the first peak of the pair bubbles with the highest point of 530 N at $\eta = 0.76$. When the bubbles are induced closer, the strong mutual interacting pair is more destructive than the combination of the impacts of single bubbles. The declining curve has the lowest point at $\eta = 1.85$ with 280 N, slightly below the second peak of 290 N, which resembles the single B1 behavior, implying that B2 slightly influences the boundary at that $\eta$ value. The second peak readings of the pair are comparable with that of the first peak for $\eta > 1.41$, where B1 and B2 are weakly affected by one another, and no B2 jet penetration on B1 appears. Beyond that $\eta$, momentous jet puncturing on B1 by B2 provokes repelling rebound bubbles at $\eta = 1.2$, hence reduced impact, and merging of collapsing bubbles before expanding again as a single cloud at $\eta < 1.2$. The elongated B1 (Fig. 6(a)) at the smallest $\eta$ has a bigger volume than B1 at $\eta = 0.98$, which elucidates the force increment at the last point. By comparison, the features of the bubbles of case B differ from case A. Note that in case B, B1 is situated far from the boundary than B2; thus, its peaks are trivial. The maximum destructive impingement (460 N) is recorded at $\eta = 1.63$ for the first peak of the pair. The equal and simultaneous opposing pressure waves generated by the coalesced tandem bubble collapse with a smaller inter bubble distance, $\eta < 1.41$, decrease the compressive stress on the boundary (Fig. 8(a)). Meanwhile, the first peaks of single B2 depict an unvarying line except at the longest distance to the boundary with 210 N. The second peak trends of pair and single B2 are analogous to each other; they decrease as $\eta$ decreases.

As previously reported in previous plots, the in-phase similar-sized bubble pairs collapse almost simultaneously, marking the sensor data with single large pulses, particularly their first and second collapses. Contrastingly, the pairs with different birth times strike the boundary

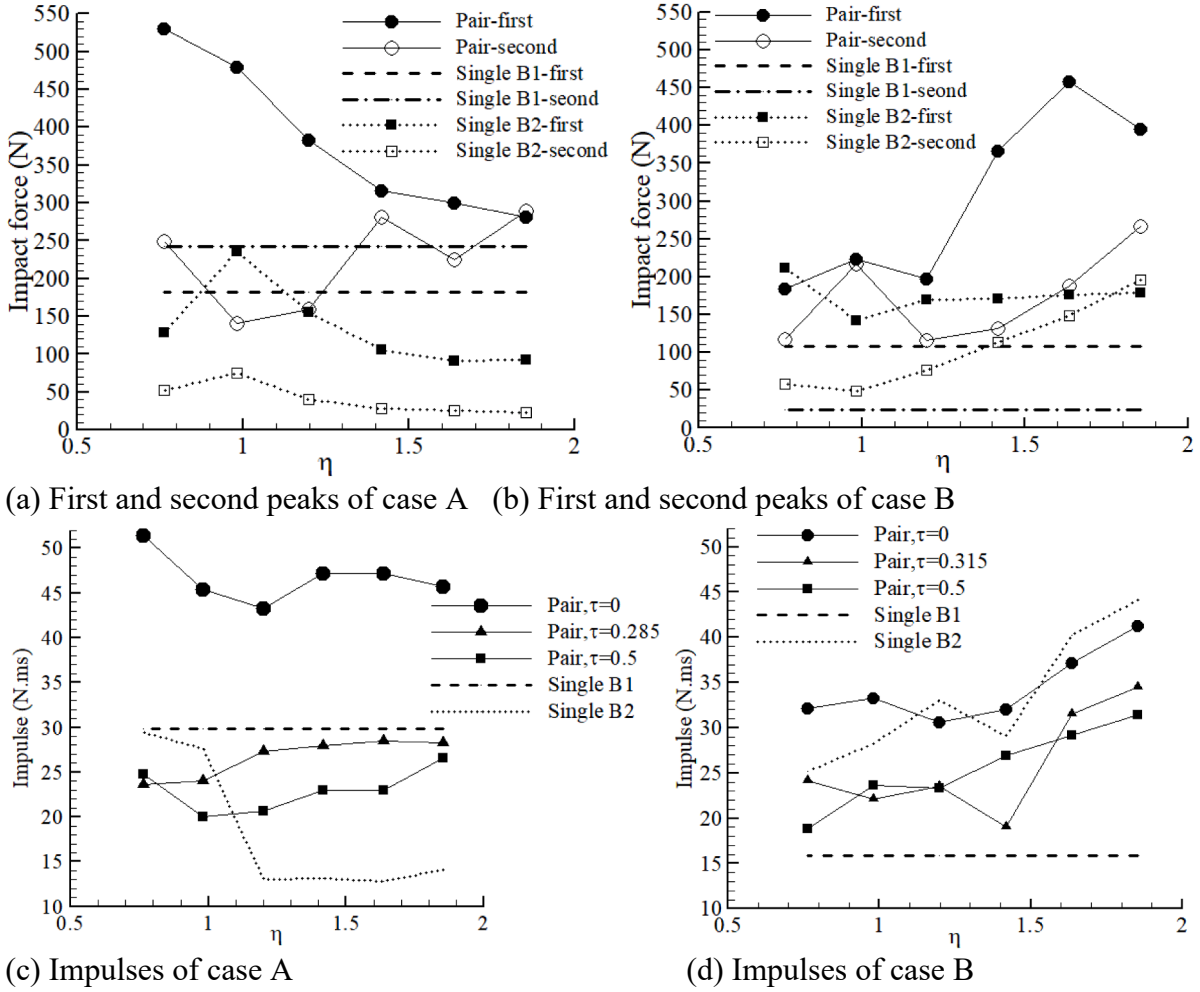


**Fig. 11.** First and second peak forces of in-phase pairs and corresponding single bubbles for cases (a) A and (b) B. Total impulses induced by in-phase pairs, out-of-phase pairs, and related single bubbles of cases (c) A and (d) B as a function of $\eta$.

with the first rising narrower pulse (collapse separately), wide pulse (resulting from collapses immediately one after another), or small bump (weak influence on the boundary). Considering that, comparing their impulses is more favorable than their peak forces. In Fig. 11(c) and (d), the total impulses acquired by the sensor are provided against $\eta$ for concurrent pairs, phase difference pairs, and single bubbles. To capture the total energy delivered during collapses, the gradual rise of the signal before the peak and the repercussion after the peak are included since these effects last longer than fast-rising pulses, regardless of their weaker strength. The largest impulse course is registered for case A sync pairs with a maximum of 51 Nms at the smallest $\eta$, and the smallest are those of single B2 (<15 Nms) excluding values of $\eta < 1$, where its strength is close to those of single B1 (~30 Nms). Evidently, the impulses of $\tau = 0.285$ are more intense than $\tau = 0.5$, although both are debilitated than single B1. When the strongest mutual interaction develops, the antiphase pair has a marginally higher measurement than the shorter $\tau$. The characteristics of case B diverge from case A since their trends do not differ much. Aside from single B1, which is the most distant; hence, the lowest impact, all features increase. When the pairs are relatively away from the boundary, $\eta = 0.76$, the largest impulse is listed by in-phase as 32 Nms, and the antiphase pair is noted as only 19 Nms. The single B1 effect is more pronounced than the sync pair for the maximum inter bubble separation. The valley at $\eta = 1.41$ when $\tau = 0.315$ matches with a single B2 response. It can be inferred that the boundary is mostly influenced by B2 than B1 at this birth time difference.

## 7. Conclusion

Herein, the interactions and resultant impulses of two axisymmetric bubbles as a function of the bubble separation distance and two arrangements (cases A and B) were investigated using a high-speed camera and a PVDF sensor and were subsequently compared. The migratory behaviors, shape deformations, jet orientations, bubble periods, and severity of collapse on the boundary were diverse and influenced by $\eta$, $\gamma$, $\tau$, and bubble placement (cases A and B). When two bubbles were created simultaneously, the jets of the pairs of case A were always oriented toward the boundary. By contrast, the pairs of case B with large ($\eta > 1.42$) and smaller ($\eta < 1.42$) gaps were directed to the boundary and toward each other, respectively. The out-of-phase pairs jetted away from one another in all cases. Concurrent pairs generally outlived the single or phase offset pairs due to the strong bubble–bubble and bubble–boundary interactions. The qualitative analysis showed that the maximum peak forces of in-phase pairs significantly exceed those of the single peaks, especially when bubbles are incepted very closely. For case A configuration, impulses of phase difference pairs were lower than in-phase pairs and single B1 values. In case B, single B2 and in-phase pairs impose greater impulse than the phase difference pairs. Moreover, it is found that the longer microjet penetration length is achieved with $\eta = 0.75$ and $\tau = 0.5$. This arrangement is favorable for cell sorting, particle displacement, or cleaning applications. Hence, it is concluded that introducing phase offset in a two-bubble system can considerably decrease the boundary damage.

## Declaration of Competing Interest

The authors declare that they have no known competing financial interests or personal relationships that could have appeared to influence the work reported in this paper.

## References


[1] Y. Tomita, A. Shima, Mechanisms of impulsive pressure generation and damage pit formation by bubble collapse, J. Fluid Mech. 169 (1986) 535–564, https://doi.org/10.1017/S0022112086000745.

[2] T. Okada, Y. Iwai, S. Hattori, N. Tanimura, Relation between impact load and the damage produced by cavitation bubble collapse, Wear. 184 (1995) 231–239, https://doi.org/10.1016/0043-1648(94)06581-0.

[3] J.-P. Franc, J.-M. Michel, Fundamentals of cavitation, Kluwer Academic Publishers, Dordrecht; Boston, 2004.

[4] I. Tzanakis, M. Hadfield, N. Garland, Cavitation damage incubation with typical fluids applied to a scroll expander system, Tribol. Int. 44 (2011) 1668–1678, https://doi.org/10.1016/j.triboint.2011.06.013.

[5] J.P. Franc, M. Riondet, A. Karimi, G.L. Chahine, Impact load measurements in an erosive cavitating flow, J. Fluids Eng. Trans. ASME. 133 (2011), https://doi.org/10.1115/1.4005342.

[6] M. Dular, T. Požar, J. Zevnik, R. Petkovšek, High speed observation of damage created by a collapse of a single cavitation bubble, Wear. 418–419 (2019) 13–23, https://doi.org/10.1016/j.wear.2018.11.004.

[7] Y.H. Chen, H.Y. Chu, L. Lin, Interaction and fragmentation of pulsed laser induced microbubbles in a narrow gap, Phys. Rev. Lett. 96 (2006) 1–4, https://doi.org/10.1103/PhysRevLett.96.034505.

[8] J. Lautz, G. Sankin, F. Yuan, P. Zhong, Displacement of particles in microfluidics by laser-generated tandem bubbles, Appl. Phys. Lett. 97 (2010) 4–7, https://doi.org/10.1063/1.3511538.

[9] G.N. Sankin, F. Yuan, P. Zhong, Pulsating tandem microbubble for localized and directional single-cell membrane poration, Phys. Rev. Lett. 105 (2010), https://doi.org/10.1103/PhysRevLett.105.078101.

[10] C.E. Brennen, Cavitation in medicine, Interface, Focus. 5 (2015) 1–12, https://doi.org/10.1098/rsfs.2015.0022.

[11] P. Cui, A.M. Zhang, S. Wang, B.C. Khoo, Ice breaking by a collapsing bubble, J. Fluid Mech. 841 (2018) 287–309, https://doi.org/10.1017/jfm.2018.63.

[12] P. Schovanec, D. Jasikova, M. Kotek, K. Havlicek, M. Nechanicka, J. Eichler, J. Cech, P. Subrtova, Sterilization of Biofilm in Foam Using a Single Cavitation Bubble, MATEC Web Conf. 328 (2020) 05003, https://doi.org/10.1051/matecconf/202032805003.

[13] H. Soyama, Laser cavitation peening and its application for improving the fatigue strength of welded parts, Metals (Basel). 11 (2021), https://doi.org/10.3390/met11040531.

[14] C.F. Hung, J.J. Hwangfu, Experimental study of the behaviour of mini-charge underwater explosion bubbles near different boundaries, J. Fluid Mech. 651 (2010) 55–80, https://doi.org/10.1017/S0022112009993776.

[15] S. Zhang, S.P. Wang, A.M. Zhang, Experimental study on the interaction between bubble and free surface using a high-voltage spark generator, Phys. Fluids. 28 (2016), https://doi.org/10.1063/1.4944349.

[16] O. Lindau, W. Lauterborn, Cinematographic observation of the collapse and rebound of a laser-produced cavitation bubble near a wall, J. Fluid Mech. (2003) 327–348, https://doi.org/10.1017/S0022112002003695.

[17] B.H.T. Goh, Y.D.A. Oh, E. Klaseboer, S.W. Ohl, B.C. Khoo, A low-voltage spark-discharge method for generation of consistent oscillating bubbles, Rev. Sci. Instrum. 84 (2013), https://doi.org/10.1063/1.4776187.

[18] A. Vogel, W. Lauterborn, R. Timm, Optical and acoustic investigations of the dynamics of laser-produced cavitation bubbles near a solid boundary, J. Fluid Mech. 206 (1989) 299–338, https://doi.org/10.1017/S0022112089002314.

[19] R.P. Tong, W.P. Schiffers, S.J. Shaw, J.R. Blake, D.C. Emmony, The role of "splashing" in the collapse of a laser-generated cavity near a rigid boundary, J. Fluid Mech. 380 (1999) 339–361, https://doi.org/10.1017/S0022112098003589.

[20] S.J. Shaw, W.P. Schiffers, D.C. Emmony, Experimental observations of the stress experienced by a solid surface when a laser-created bubble oscillates in its vicinity, J. Acoust. Soc. Am. 110 (2001) 1822–1827, https://doi.org/10.1121/1.1397358.

[21] E.A. Brujan, G.S. Keen, A. Vogel, J.R. Blake, The final stage of the collapse of a cavitation bubble close to a rigid boundary, Phys. Fluids. 14 (2002) 85–92, https://doi.org/10.1063/1.1421102.

[22] Y.C. Wang, C.H. Huang, Y.C. Lee, H.H. Tsai, Development of a PVDF sensor array for measurement of the impulsive pressure generated by cavitation bubble collapse, Exp. Fluids. 41 (2006) 365–373, https://doi.org/10.1007/s00348-006-0135-8.

[23] Y.C. Wang, Y.W. Chen, Application of piezoelectric PVDF film to the measurement of impulsive forces generated by cavitation bubble collapse near a solid boundary, Exp. Therm. Fluid Sci. 32 (2007) 403–414, https://doi.org/10.1016/j.expthermflusci.2007.05.003.

[24] X. Yao, X. Cui, K. Guo, Y. Chen, An Experimental Approach to the Measurement of Wall Pressure Generated by an Underwater Spark-Generated Bubble by a Hopkinson Bar, Shock Vib. 2019 (2019), https://doi.org/10.1155/2019/5341317.

[25] S.R. Gonzalez-Avila, F. Denner, C.D. Ohl, The acoustic pressure generated by the cavitation bubble expansion and collapse near a rigid wall, Phys. Fluids. 33 (2021), https://doi.org/10.1063/5.0043822.

[26] Y. Tomita, P.B. Robinson, R.P. Tong, J.R. Blake, Growth and collapse of cavitation bubbles near a curved rigid boundary, J. Fluid Mech. 466 (2002) 259–283, https://doi.org/10.1017/S0022112002001209.

[27] J. Cui, Z.P. Chen, Q. Wang, T.R. Zhou, C. Corbett, Experimental studies of bubble dynamics inside a corner, Ultrason. Sonochem. 64 (2020), 104951, https://doi.org/10.1016/j.ultsonch.2019.104951.

[28] E.A. Brujan, K. Nahen, P. Schmidt, A. Vogel, Dynamics of laser-induced cavitation bubbles near an elastic boundary, J. Fluid Mech. 433 (2001) 251–281, https://doi.org/10.1017/S0022112000003347.

[29] G. Huang, M. Zhang, X. Ma, Q. Chang, C. Zheng, B. Huang, Dynamic behavior of a single bubble between the free surface and rigid wall, Ultrason. Sonochem. 67 (2020), 105147, https://doi.org/10.1016/j.ultsonch.2020.105147.

[30] J.R. Blake, P.B. Robinson, A. Shima, Y. Tomita, Interaction of two cavitation bubbles with a rigid boundary, J. Fluid Mech. 255 (1993) 707–721, https://doi.org/10.1017/S0022112093002654.

[31] B. Han, K. Köhler, K. Jungnickel, R. Mettin, W. Lauterborn, A. Vogel, Dynamics of laser-induced bubble pairs, J. Fluid Mech. 771 (2015) 706–742, https://doi.org/10.1017/jfm.2015.183.
[32] Y. Tomita, K. Sato, Pulsed jets driven by two interacting cavitation bubbles produced at different times, J. Fluid Mech. 819 (2017) 465–493, https://doi.org/10.1017/jfm.2017.185.
[33] V. Robles, E. Gutierrez-Herrera, L.F. Devia-Cruz, D. Banks, S. Camacho-Lopez, G. Aguilar, Soft material perforation via double-bubble laser-induced cavitation microjets, Phys. Fluids. 32 (2020), 042005, https://doi.org/10.1063/5.0007164.
[34] J. Hujer, M. Müller, P. Dančová, Calibration of PVDF Film Transducers for the Cavitation Impact Measurement, EPJ Web Conf. 180 (2018) 02036.